Effects of process parameters and annealing on microstructure and properties of CoCrFeMnNi high-entropy alloy coating prepared by plasma cladding

**Shi-yong Wei[1], Chao-min Wang[1], *Wen-yi Peng[2], Ru-kai Luo[2], Yun Chen[1], Zhen-zhen Wan[1], and Yin Jin[1]

1. Institute of Applied Physics, Jiangxi Academy of Sciences, Nanchang 330090, China
2. Materials Science and Engineering School, Nanchang University, Nanchang 330029, China

Abstract: Plasma cladding was used to prepare a CoCrFeMnNi high-entropy alloy (HEA) coating under different conditions. The process parameters were optimized using an orthogonal experiment design based on surface morphology quality characteristics, dilution rate, and hardness. The optimal process parameters were determined through range and variance analysis to be a cladding current of 70 A, a cladding speed of 7 cm·min^{-1}, and a powder gas flow rate of 8 L·s^{-1}. During the optimized experiments, both the cladded and annealed CoCrFeMnNi HEA coatings exhibit some pores, micro-voids, and a small amount of aggregation. However, the aggregation in the annealed coating is more dispersed than that in the cladded coating. The cladded CoCrFeMnNi HEA coating consists of simple FCC phases, while a new Cr-rich phase precipitates from the FCC matrix after annealing the coating at a temperature range of 550 °C–950 °C. After annealing at 850 °C, the proportion of the FCC phase decreases compared to the cladded coating, and the number of large-angle grain boundaries is significantly reduced. However, the proportion of grains with sizes below 50 μm increases from 61.7% to 74.3%. The micro-hardness and wear resistance of the cladded coating initially increases but then decreases with an increase in annealing temperature, indicating that appropriate annealing can significantly improve the mechanical properties of the CoCrFeMnNi HEA coatings by plasma cladding. The micro-hardness of the CoCrFeMnNi HEA coatings after annealing at 650 °C increases to 274.82 HV$_{0.2}$, while the friction coefficient decreases to below 0.595.

Keywords: plasma cladding; CoCrFeMnNi HEA coating; process optimization; annealing; microstructure and mechanical property

CLC numbers: TG142.31   Document code: A   Article ID: 1672-6421(2023)06-491-12

1 Introduction

High entropy alloys (HEAs) have garnered significant attention due to their unique characteristics, including high entropy, sluggish diffusion, severe lattice distortion, and cocktail effects. These properties contribute to outstanding mechanical performance such as high strength, high ductility, excellent wear resistance, corrosion resistance, and more [1-3]. Despite these advantages of HEAs, their utilization has been limited by constraints in size and shape during preparation. Additionally, the higher cost associated with using more expensive elements in HEAs compared to conventional alloys has hindered their widespread adoption across various applications [4]. Recently, the high-performance HEA coatings are attracting increasing attention, since their cost has been reduced due to their much thinner thickness and wider industrial application [5]. Generally, relatively thick and dense HEA coatings with good metallurgical bonding to the substrate are suitable for structural application because such coatings can withstand aggressive attack loads.

Plasma cladding is an effective fabrication approach for obtaining HEA coatings. Compared to the conventional methods such as arc welding, physical or chemical vapor deposition, and thermal spraying, the HEA coatings obtained by plasma cladding exhibit better mechanical properties, better metallurgic bonding, and fewer metallurgic defects [6-8]. Many studies have been conducted to investigate the influence of process parameters on the plasma cladding properties. Wei et al. [9] obtained WC/Ni-based composite coating by plasma

cladding, and used an orthogonal design of experiment to investigate the mapping relationships between the as-deposited coating characteristics (surface roughness, thickness, volume fraction of tungsten carbides) and the process parameters. The results showed that welding current, powder feeding rate, and welding speed had significant influence on degradation of the tungsten carbide. Wang et al. [10] studied the distribution of residual stress of a Co-based coating by plasma cladding under different process parameters. The working current was found to be the most significant influence factor on the residual stress.

Plasma cladding is a widely used technique for preparing self-fluxing alloy coatings such as iron-based, nickel-based, and cobalt-based coatings, as well as their composite coatings. Recent studies have primarily focused on the influences of plasma cladding parameters on mechanical properties of these coatings [11-13]. However, there has been few research works on the optimization of the plasma cladding process parameters for HEA coatings. In order to achieve the desired characteristics of HEA coatings, it is important to optimize the plasma cladding process parameters. This can be done by studying the effect of parameters such as powder feeding gas flux, cladding current, and cladding speed on the coating characteristics. In addition, it is well-known that plasma cladding is a rapid heating and cooling process, residual stress is often present in the cladding layer. Therefore, it is essential to select an appropriate annealing process.

Among many high-entropy alloy systems, CrCoFeNiMn high-entropy alloy is one of the earliest proposed and studied high-entropy alloys with a stable face-centered cubic (FCC) structure. As the temperature decreases, the high-entropy alloy exhibits no ductile-brittle transition, and both of its strength and toughness increase. At 77 K, under the action of nano-scale deformation twins, the tensile strength can reach 1,280 MPa, and the elongation exceeds 70% [14]. It is one of the low-temperature materials with the most development potential and application prospects, and can be used in the field of surface coating repair and remanufacturing. Several researchers have discovered that a second phase tends to precipitate during medium-temperature annealing of the CoCrFeMnNi high-entropy alloy [15-17]. Otto et al. [14] found that the CoCrFeMnNi high-entropy alloy was unstable, leading to the formation of second-phase precipitates during annealing at 700 and 500 °C. The Cr-rich σ phase precipitated between grains at 700 °C, while at 500 °C, the Cr-rich BCC phase, L10-NiMn, and B2-FeCo precipitated between grains. Sathiyamoorthi et al. [15] observed the presence of the σ-phase after annealing at 700 °C for 1 h, and the σ phase showed slightly higher concentration of Cr and Mn compared to the FCC matrix. Wang et al. [16] studied the effects of annealing process parameters on microstructural evolution and strength-ductility combination of CoCrFeMnNi high-entropy alloy. The results showed that a typical heterogeneous structure composed of the ultra-fine grains in nano/submicron scale and coarse grains could be obtained by annealing at 873–923 K. Excessive annealing time results in a reduction in the content of ultra-fine grains and diminishes the mechanical compatibility between soft and hard zones. Therefore, it is crucial to control the holding time in order to retain more ultra-fine grains within the heterogeneous structure, which leads to a superior combination of strength and ductility. However, few studies can be found concerning the effect of parameters optimization and annealing on comprehensive characteristics of CoCrFeMnNi HEA prepared by plasma cladding.

In this study, CoCrFeMnNi HEA coatings were manufactured on Q235 steel by plasma cladding. The process parameters were optimized by orthogonal method for obtaining the optimal characteristics of the coatings. Moreover, the effect of annealing temperatures on the evolution of phase, microstructure, and mechanical properties of CoCrFeMnNi HEA coatings was also investigated systematically. These findings are expected to provide valuable insights for the preparation of high-entropy alloy (HEA) coatings.

2 Experimental materials and methods

2.1 Experimental materials

Q235 carbon steel, with a composition range of (0.14–0.22)wt.% C, (0.30–0.65)wt.% Mn, ≤0.30wt.% Si, ≤0.05wt.% S, and ≤0.45wt.% P (Fe is the balance), was chosen as the substrate material for this study. The dimensions of the substrate were 200 mm×200 mm×10 mm. CoCrFeMnNi HEA powder with approximately equimolar ratio was fabricated by gas atomization, as shown in Fig. 1(a). The size of powder particles was measured using the Nano Measurer 1.2, a minimum of 100 particles were measured. The average size of the HEA powder particles was approximately 18.48 μm, with a size distribution ranging from 7.47 to 38.23 μm [Fig. 1(b)].

2.2 Experimental method

Prior to cladding, the plates were cleaned with emery papers to remove the oxidized layer. Cladding was performed on all of the samples using a plasma cladding test machine. During the plasma cladding process, high-purity argon gas was selected as the source for plasma generation, shielding, and powder feeding. In the orthogonal experiment, plasma cladding process parameters such as oscillation width, oscillation rate, and the flux of the plasma and shielding gas were set to constant values (Table 1). While, the process parameters including cladding current, cladding speed, and powder feeding gas flux were set in 3 levels, as shown in Table 2. Then, a L_9 (3^3) orthogonal array was designed to investigate the influence of the cladding current, cladding speed, and powder feeding gas flux on the microstructure and properties of the cladding coatings. The optimization of the process parameters was performed to obtain the cladding coatings with good macroscopic morphology, a moderate dilution rate, and a high hardness.

An optical microscope (OM) was used to observe the surface and cross-sectional morphologies. The surface hardness of the coatings was evaluated using an Vickers hardness test instrument with a load of 1.96 N for 15 s (0.5 mm spacing
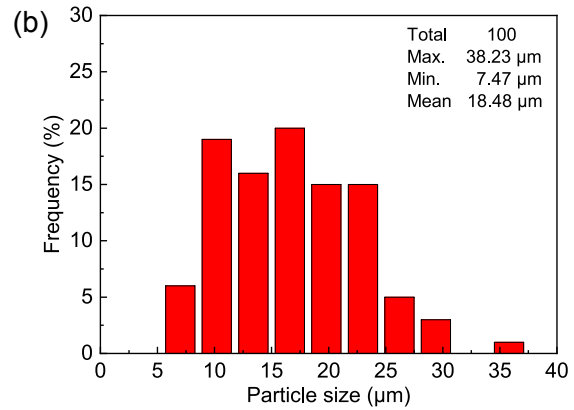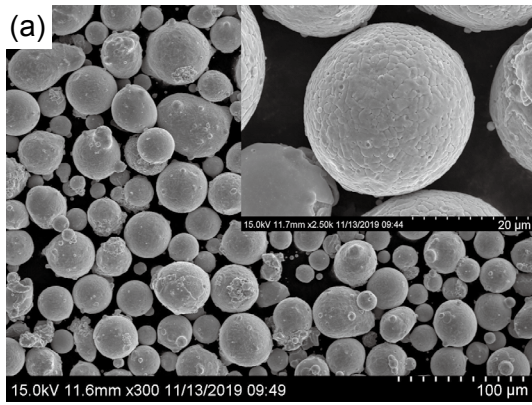
Fig. 1: CoCrFeMnNi HEA powder: (a) SEM; (b) particle size distribution

Table 1: Cladding parameters during plasma cladding process

Parameters	Value
Oscillation width (mm)	8.0
Oscillation speed (mm·s⁻¹)	10.0
Plasma gas flux (L·s⁻¹)	1.2
Shielding gas flux (L·s⁻¹)	1.0

Table 2: Orthogonal factors and levels

Levels	Factors		
	A	B	C
	Cladding current (A)	Cladding speed (cm·min⁻¹)	Powder feeding gas flux (L·s⁻¹)
1	60	3	6
2	70	5	8
3	80	7	10

between the test points). The dilution rate (γ) can be calculated by the following Eq. (1) [18]:

$$\gamma = \frac{b}{h+b} \qquad (1)$$

where γ is the dilution rate, b is the penetration depth of the substrate, mm; and h is the height of the coating, mm, as shown in Fig. 2.

The samples prepared with optimized parameters were cut into a rectangular specimen measured 10 mm×10 mm×5 mm using a wire electrical discharge machine, and divided into two groups. The samples in one group were cladded samples; while the
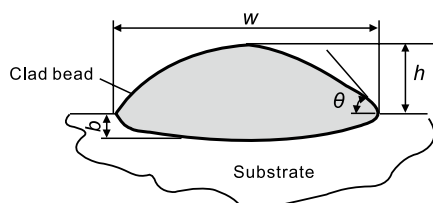

Fig. 2: Measurement of the cladding layer dilution rate

samples in the other group were annealed samples. It was reported that the σ phase precipitated in a temperature range of 650 °C to 800 °C, and dissolved at about 850 °C to 950 °C [19]. Therefore, the annealing temperature was set at 550, 650, 850, 950 and 1,050 °C, respectively, whereas the annealing time was set to 4 h. The samples were heated in a tube vacuum furnace and then cooled down in the atmosphere.

The cladded and the annealed samples were ground with sandpapers, polished, followed by etched with aqua-regain (HCl:HNO₃=3:1, volume ratio) for 15–30 s. The phase constitutions of the coating were analyzed using an X-ray diffraction (XRD) with Cu Ka radiation at a scanning speed of 5 °·min⁻¹. The microstructure, element distribution and powder morphology of the coating samples were investigated using a scanning electron microscope (SEM) equipped with an energy dispersive spectrometer (EDS). In addition, electron backscatter diffraction (EBSD) measurements were performed at an acceleration voltage of 20 kV, and the EBSD images were obtained using the Oxford HKL Channel5 software. The ball-on-disk wear tester was used for wear testing at room temperature, and the parameters used in the test were as follows: a Si₃N₄ ceramic ball with a diameter of 4 mm, the load of 5 N, frequency of 10 Hz (560 r·min⁻¹), friction radius of 5 mm, and duration time of 30 min.

3 Results and discussion

3.1 Optimization of process parameters

Figure 3 shows the macroscopic morphology of the single-track CoCrFeMnNi HEA coating samples S1–S9. It is observed that the three factors play an important role in determining the quality of the CoCrFeMnNi HEA coatings. Figures 3(a–c) show that Samples 1–3 exhibit numerous macro-cracks at the coating end (red circle in Fig. 3) when the cladding current is set to a low level (60 A). This phenomenon can be attributed to insufficient input energy, which results in a lack of metallurgical bonding at the interface between the cladded coating and substrate. Sticky powder is found on the surfaces of Samples 4, 6 and 7, as shown in Figs. 3(d, f and g). In addition, Sample 5 exhibits cladding defects on its surface, such as pits and uneven cladding, as shown in Fig. 3(e). Nevertheless, the thickness of

Samples 8 and 9 is relatively thinner and obvious oxidation occurs, as shown in Figs. 3(h) and (i).

The dilution rate, hardness and macroscopic defects of coatings [11] were chosen as the three check indexes of coating quality. The results of the test and range analysis of Samples 1 to 9 in Fig. 3 are presented in Table 3.

The resulting response graph between process parameters and factors is shown in Fig. 4. The optimal process parameters for plasma cladding (according to the range analysis for the dilution rate with a moderate value) are A2, B2, and C2: cladding current (70 A), cladding speed (5 cm·min⁻¹), and powder feeding gas flow (8 L·s⁻¹). But, according to range analysis for hardness with a high value, the optimal combination of parameters are A1, B3, and C2: cladding current (60 A), cladding speed (7 cm·min⁻¹), and powder feedidng gas flow (8 L·s⁻¹).

To further confirm the appropriate process parameters, the factors and levels were analyzed by variance, as presented in Table 4. Where S is the sum of square of deviatirons, f is the degree of freedom, and MS/f is the mean square. Variance results for the dilution rate indicate that the F values of Factors A (cladding current), B (cladding speed) and C (powder gas flow) are 6.69, 7.99, and 0.10, respectively, indicating that they are not significant factors with regard to their effects on the dilution rate of coatings comparing to $F_{0.01}$. However, according to the variance analysis for hardness, the F value of Factors A, B and C are 310.64, 35.30, and 9.32, respectively, indicating that Factor A is a significant factor with regard to its effects on the hardness of the coatings compared with $F_{0.01}$. In addition, if the F_α is set to $F_{0.05}$, Factors A and B show significant effects on the hardness of coatings. When F_α was set to $F_{0.1}$, Factors A, B, and C are all have significant effects on the hardness of the coatings.
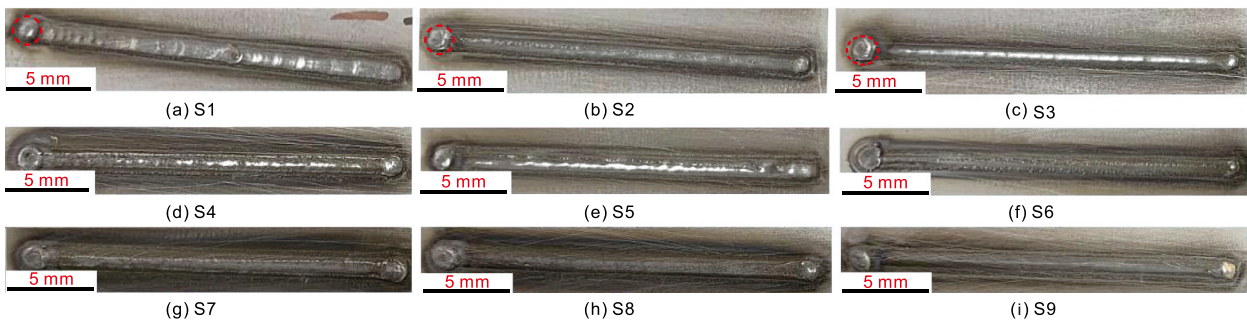

Fig. 3: Macroscopic morphologies of cladded samples with different processing parameters (a–i)

Table 3: Orthogonal test results and range analysis

Sample No.	A (A)	B (cm·min⁻¹)	C (L·s⁻¹)	Dilution rate (%)	Hardness−150 (HV)	Defect
S1	60	3	6	18.37	25.7	Macro-crack
S2	60	5	8	15.52	30.5	Macro-crack
S3	60	7	10	9.43	37.1	Macro-crack
S4	70	5	10	16.81	1.5	Sticky powder
S5	70	7	6	13.02	−6.0	Pit
S6	70	3	8	29.34	16.8	Sticky powder
S7	80	7	8	17.86	−10.7	Sticky powder
S8	80	3	10	38.32	−12.2	Oxidation
S9	80	5	6	28.12	−4.4	Shallow cladding

Range analysis:

	Dilution rate — A	B	C		Hardness — A	B	C
K_1	43.32	86.03	59.51	K_1	93.3	16.5	15.3
K_2	59.17	60.45	62.72	K_2	12.3	12.3	36.6
K_3	84.30	40.31	64.56	K_3	−27.3	49.5	26.4
κ_1	14.44	28.67	19.84	κ_1	31.1	5.5	5.1
κ_2	19.72	20.15	20.91	κ_2	4.1	4.1	12.2
κ_3	28.10	13.43	21.52	κ_3	−9.1	16.5	8.8
R	13.66	15.24	1.68	R	40.2	12.4	7.1
Optimization	A_2	B_2	C_2	Optimization	A_1	B_3	C_2

Experiments were performed to confirm the validity of the orthogonal test results. According to Table 4, Factor B has a more significant effect on the hardness than the dilution rate, so that B3 (7 cm·min⁻¹) is more reliable. In addition, according to the macroscopic morphology of the CoCrFeMnNi HEA coatings in Fig. 3, when Factor A is 60 A, the coating samples show many macroscopic cracks. Therefore, A2 is more appropriate. Comprehensive analysis of the range and variance shows that the optimal process parameters of plasma cladded CoCrFeMnNi HEA coatings are A2, B3 and C2, therefore, the best parameters of cladding current, cladding speed, and powder feeding gas flow rate are determined to be 70 A, 7 cm·min⁻¹, and 8 L·s⁻¹, respectively.

3.2 Surface and cross-sectional morphology

Figure 5(a) shows the surface morphology of the samples cladded using optimal parameters with double-track. It is found that the surface of the CoCrFeMnNi HEA coating is smooth and has no obvious macro-defects. The cross-sectional morphology of the coating presents a wave curve shape of the bonding line, as shown in Fig. 5(b). Additionally, the dilution rate of the CoCrFeMnNi HEA coating is 18.01% according to Eq. (1). In plasma arc welding, a dilution rate range of 5%–30% is generally considered reliable [19]. This implies that the quality characteristics of CoCrFeMnNi coating are significantly affected by the optimal process parameters.
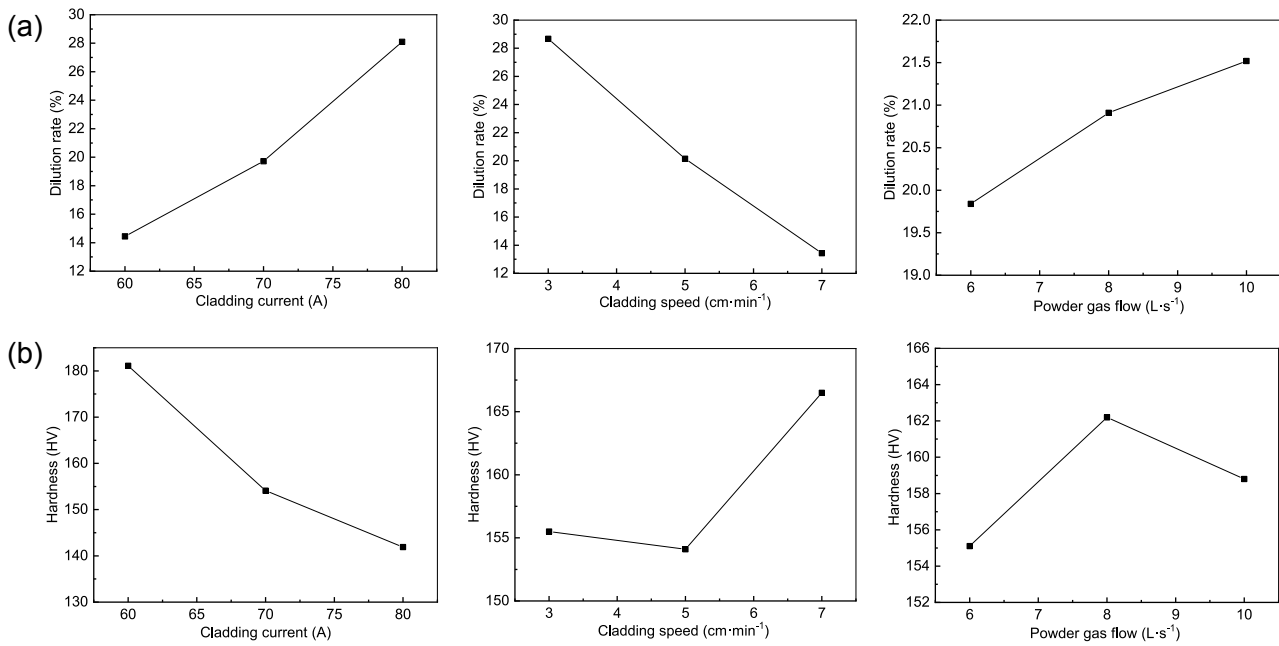

Fig. 4: Response graph between dilution rate (a) and hardness (b) and factors

Table 4: Variance analysis of dilution rate and hardness

Index	Sources	S	f	MS/f	F value	Critical F value	Significant
Dilution rate	A	284.68	2	142.34	6.69		–
	B	350.03	2	170.01	7.99		–
	C	4.36	2	2.18	0.10	$F_{0.1}$ (2,2)=9	–
	E_s	42.53	2	21.27			
	Sum T	681.6	8				
Hardness	A	2,519.28	2	1,259.64	310.64	$F_{0.01}$ (2,2)=99	**
	B	286.07	2	143.35	35.30	$F_{0.05}$ (2,2)=19	*
	C	75.66	2	37.83	9.32	$F_{0.1}$ (2,2)=9	
	E_s	8.11	2	4.06			
	Sum T	2 889.12	8				

Note: F_α is the critical value found in the F distribution table, and the α is the test level. In general, if $F>F_{0.01}$, the influence of this factor is said to be highly significant, which is indicated by two asterisk (**). If $F_{0.05}<F<F_{0.01}$, the factor is said to be significant and is indicated by an asterisk (*). If $F<F_{0.05}$, it is said to be insignificant.

3.3 Phase identification

Figure 6 shows the XRD patterns of the cladded and annealed CoCrFeMnNi HEA coatings. It indicates that the main crystalline structure in the CoCrFeMnNi coatings is a simple FCC lattice structure. The diffraction angles of the cladded coatings at the diffraction peaks are 43.594°, 50.694°, 74.615° and 90.413°, respectively, which are consistent with the results by Ye et al [20]. After annealed at 550 °C, the (111) peak weakens and the intensities of the other diffraction peaks of the FCC phase increase. An additional peak of the BCC phase is detected in the sample annealed at 650 °C, while the (111) and (220) peaks become very weak and could hardly be identified; the relative intensity of the (200) peak, however, increases significantly. After annealing at 850 °C and 950 °C, the FeCr phase diffraction peak appears in the coatings, and Cr-rich precipitates are observed on the grain boundaries [Figs. 7(d) and (e)], which is consistent with the results by He et al [21]. Nevertheless, when the annealing temperature reaches 1,050 °C, the peaks of the sample are still indicating a single FCC solid solution phase. This phenomenon indicates that the BCC and FeCr phases are thermodynamically unstable structures, and the formation of the FCC phase is closely related to the dissolution of BCC and FeCr phases at high temperatures [22].

3.4 Microstructure characterization

Figure 7 shows the cross-sectional SEM images of the cladded and annealed CoCrFeMnNi alloy coatings. It is observed that the cladded coating is mainly consisted of dendrites (DR) and interdendrites (IR), as shown in Fig. 7(a). After annealing, the dendrites of the annealed coating grow with an increase in annealing temperature. Moreover, when the annealing temperature exceeds 550 °C, the recrystallized grain structure is observed, as shown in Figs. 7(b–e). The compositions of different microstructures were analyzed by EDS, and the results are shown in Table 5. It can be seen that the content of Fe in all the coatings is higher than that of other elements except Regions 2 and 8, possibly due to the diffusion of the substrate elements.
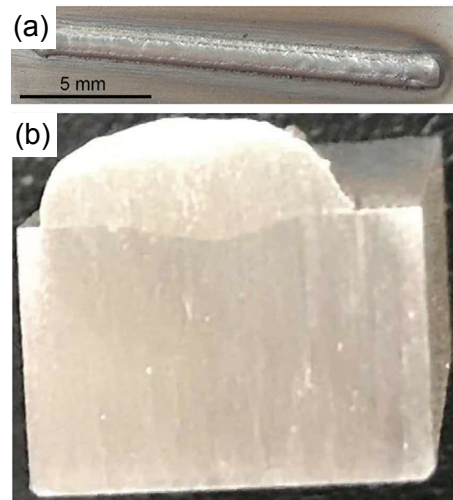

Fig. 5: Surface (a) and cross-section (b) morphology of optimal CoCrFeMnNi HEA coating
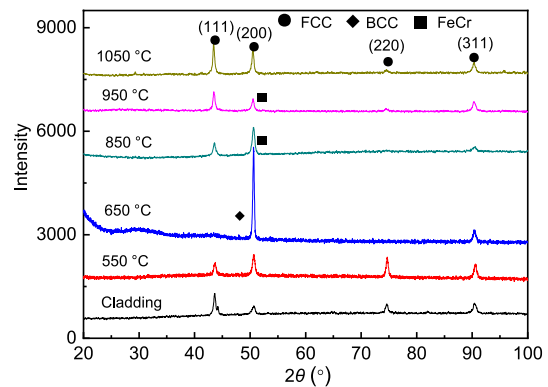

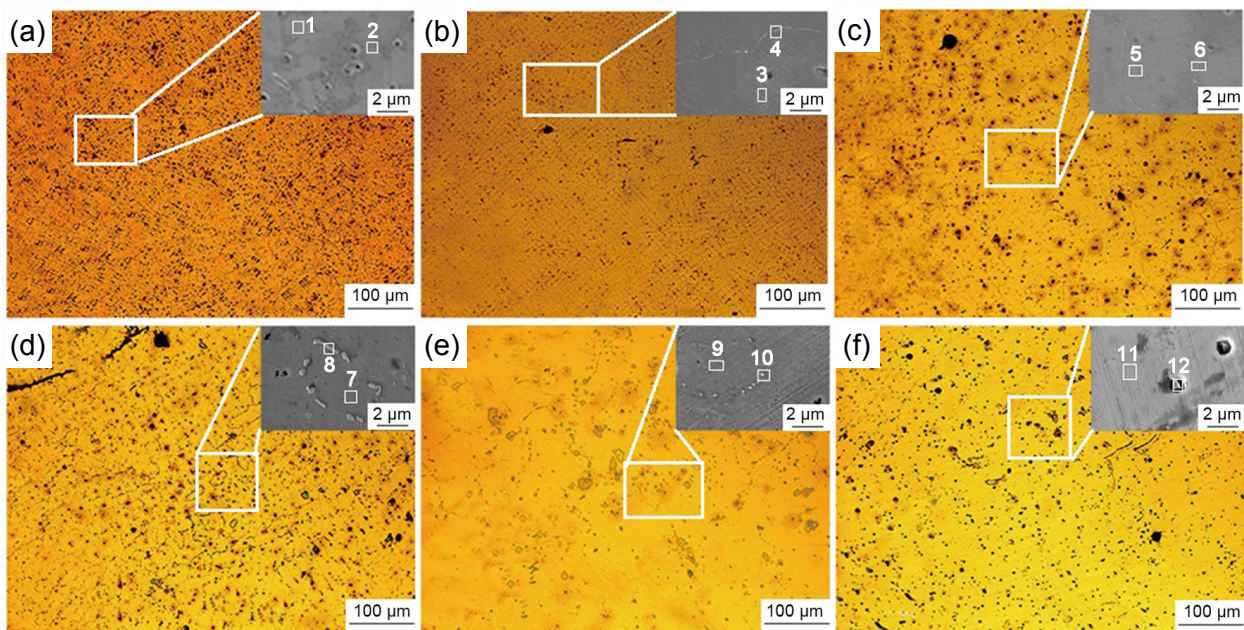**Fig. 6: XRD patterns of cladded and annealed coatings**

Fig. 7: SEM images of cladded and annealed CoCrFeMnNi HEA alloy coatings: (a) cladded; (b) 550 °C; (c) 650 °C; (d) 850 °C; (e) 950 °C; (f) 1,050 °C

Figure 8 shows the defect distributions on the surfaces of both the cladded and the 850 °C annealed HEA coatings. It is observed that some process defects such as large-size circular pores and micro-voids are formed on the surfaces of the cladded and the annealed coatings [Figs. 8(a, b)]. However, the number of micro-voids in the annealed coating is decreased [Fig. 8(b)] because high temperature and long time provide enough driving force for the residual gas to escape from the annealed coatings [23]. In addition, a small amount of aggregations are observed on the surface of both coatings. Under the plasma cladding process, alloying and solidification processes of the high-entropy alloy molten pool are very complex. Among the elements of CoCrFeMnNi HEA, manganese (Mn) has the lowest boiling point of 1,962 °C, while the boiling points of the other elements are all above 2,700 °C. Consequently, Mn is more likely to vaporize and form bubbles and pores during the plasma cladding process. At the same time, some metal elements are oxidized at high temperature, and segregated in the form of oxides. During plasma cladding, the solidification rate is significantly high, thus resulting in numerous small bubbles that are unable to overflow or coalesce [24].

Furthermore, due to the Gaussian distribution of the plasma, melting starts at the surface of the intermediate aggregations, and the gravity and fluidity of the molten metal after melting lead to heat transfer [25]. Therefore, aggregations are seen to have converged on the surface of the coating, as depicted in Fig. 8. The aggregations are more concentrated in the cladded coatings than in the annealed coatings, indicating that some aggregations are dissolved or decomposed with the diffusion or replacement of the elements during the annealing process [26]. The aggregations (Points A and C in Fig. 8) and the coating matrix (Points B and C in Fig. 8) were analyzed by ESD, and the results are presented in Table 6. It is observed that the contents of the main elements in the coating matrix show no evident changes between the cladded and the annealed coatings, but clear difference is observed for the aggregations. The contents of main elements in aggregations of annealed coating are lower than that of the cladded coating, maybe due to that during the annealing process, the diffusion activation energy of atoms increases, and the solid solution of carbides or oxides dispersion can also contribute to the decrease in aggregation [26-27].

Table 5: EDS point scanning results of cladded and annealed coatings (at.%)

| Conditions	Regions	Co	Cr	Fe	Mn	Ni
Cladding	1	21.12	18.66	26.03	16.13	18.06
	2	17.24	17.04	19.11	24.46	20.30
550 °C	3	17.32	18.29	25.83	20.49	18.07
	4	17.56	18.25	26.32	19.88	18.00
650 °C	5	19.39	19.38	30.64	14.81	15.78
	6	18.80	15.75	29.88	15.75	16.42
850 °C	7	16.96	17.58	27.86	20.00	17.61
	8	14.32	30.54	26.92	15.44	12.78
950 °C	9	19.42	17.79	27.95	17.58	17.27
	10	17.00	21.27	23.46	19.49	18.77
1,050 °C	11	19.55	16.99	26.54	18.18	18.74
	12	18.66	17.99	26.64	19.16	17.56
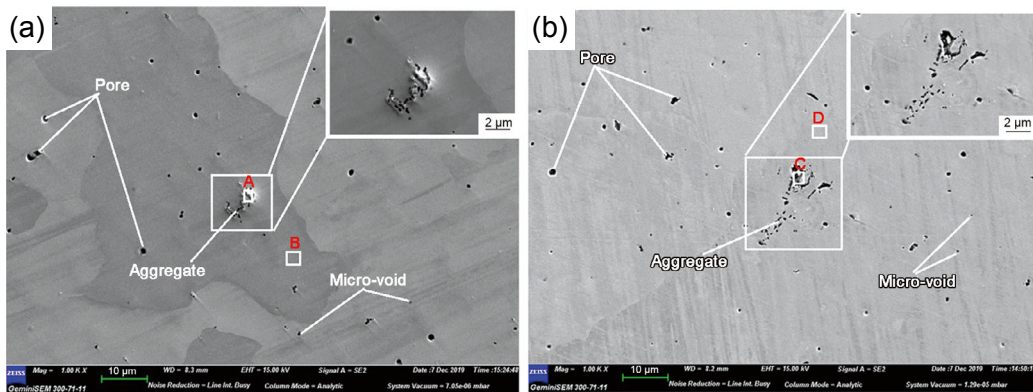
Fig. 8: SEM images of surface of HEA coatings: (a) cladded; (b) annealed at 850 °C

Table 6: EDS points scanning of aggregations and matrix on the surface of HEA coatings at different states (at.%)

Positions	Co	Cr	Fe	Mn	Ni	Impurity elements				
						Al	C	O	Si	S
A	8.5	9.0	9.4	12.6	11.3	11.5	19.3	18.2	0.2	–
B	13.7	14.9	15.0	17.3	15.1	0.3	23.7	–	–	–
C	6.6	6.3	7.5	10.5	9.6	8.5	35.1	15.0	0.8	0.2
D	14.2	14.4	17.3	15.6	14.9	0.2	23.2	–	0.2	–

Figure 9 shows the EBSD phase fraction of the cladded and the 850 °C annealed HEA coatings. There are only FCC and a few unknown phases. The fractions of the FCC phase in the cladded and annealed coating are 98.27% and 92.09%, respectively [Figs. 9(a and b)], indicating that the annealing treatment could reduce the FCC phase content. Nevertheless, the content of the unknown phase is clearly increased in the annealed coating, possibly because the Cr-rich phase could not be detected by EBSD.

Figure 10 shows the grain boundaries and the distribution of the misorientation of the HEA coatings that cladded and annealed at 850 °C. As shown in Figs. 10(a) and (c), the green and black lines represent the low-angle grain boundaries (LAGBs, with misorientation between 0° and 15°) and the high-angle grain boundaries (HAGBs, with misorientation greater than 15°) in the coatings, respectively. Comparison of Figs. 10(b) and (d) shows that annealing treatment leads to a significant decrease in the number of the HAGBs in the CoCrFeMnNi HEA coating. This implies that a higher density of sub-grains or twins is formed in the annealed HEA coatings.

Figure 11 shows the EBSD inverse pole figure (IPF) maps and grain size distribution of the cladded and the 850 °C annealed HEA coatings. It is observed that the microstructures of the cladded coating are composed of many fine grains and a few columnar and massive grains [Fig. 11(a)]. More small grains appear in the annealed coatings [Fig. 11(c)]. This is mainly due to the effects of the precipitated particles on the grain boundaries during the annealing process [28]. After annealing treatment at 850 °C, the proportion of the grains with a size of less than 50 μm increases from 61.7% to 74.3%, as shown in Figs. 11(b) and 10(c). This suggests that the effect of grain refinement through appropriate annealing is significant.

3.5 Mechanical properties

Figure 12 shows the microhardness of the surface of the CoCrFeMnNi HEA coatings at different annealing temperatures. The average microhardness of the annealed coatings are 266.0, 274.8, 255.2, 242.9, and 240.8 $HV_{0.2}$, respectively, which are higher than that of the cladded coating (216.7 $HV_{0.2}$). It is observed that the microhardness increases at first and then decreases with an increase in annealing temperature. The highest microhardness of 274.8 $HV_{0.2}$ is obtained for the coating annealed at 650 °C.

Figure 13 shows the friction coefficient curves of the cladded and the annealed CoCrFeMnNi HEA coatings. It is observed that the friction coefficient almost reaches the steady state after sliding for 5 min. The average friction coefficient values of the cladded coating and the coatings after annealed at 550 °C, 650 °C, 850 °C, 950 °C, and 1,050 °C are approximately 0.788, 0.674, 0.595, 0.599, 0.609, and 0.743, respectively. Thus, it can be concluded that the friction coefficient firstly decreases and then increases with an increase in annealing temperature. Similar to the above results for the microhardness, the coating annealed at 650 °C shows a lowest friction coefficient value. In addition, the fluctuations of the friction coefficient curves (Fig. 13) indicate that the friction coefficient may be affected by grain orientation, grain size and component segregation [29].

Figure 14 shows the wear loss of the cladded and annealed CoCrFeMnNi HEA coatings. The wear loss values of the cladded coating and the coatings annealed at 550 °C, 650 °C, 850 °C, 950 °C, 1,050 °C are 1.98, 1.46, 1.12, 1.23, 1.35, and 1.64 mg, respectively. It is observed that the wear loss of annealed coatings is lower than that of the cladded coating under the identical conditions.
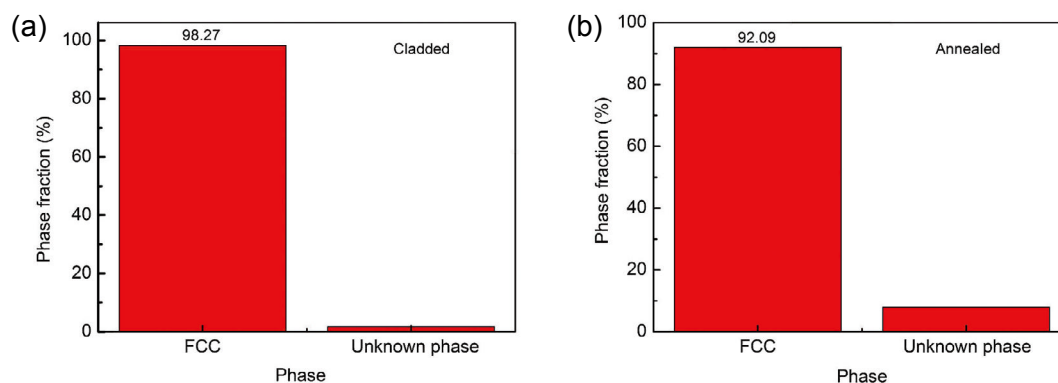

Fig. 9: Phase fraction of HEA coatings by EBSD: (a) cladded; (b) annealed at 850 °C
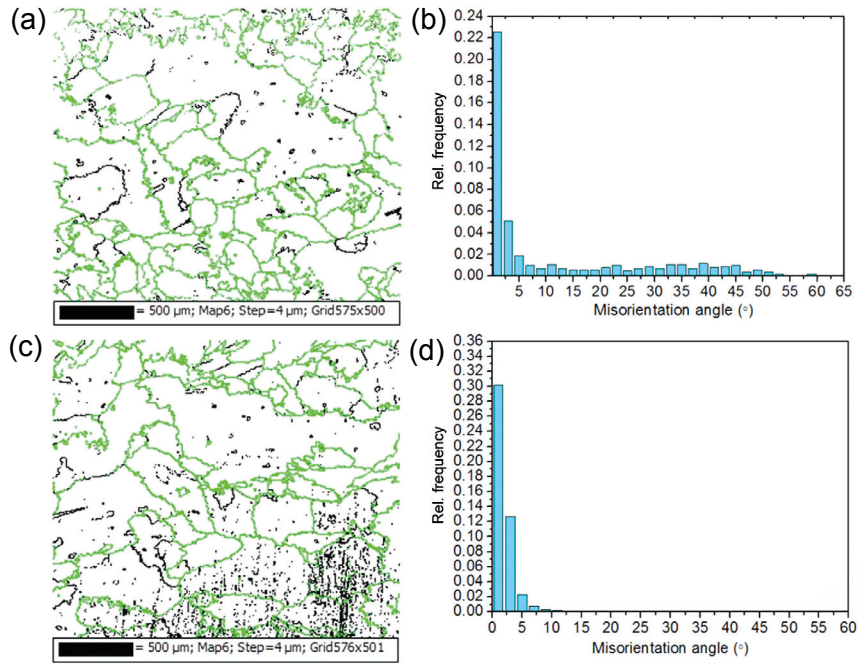
Fig. 10: Grain boundary and distribution of misorientation of HEA coatings: (a) and (b) cladded; (c) and (d) annealed at 850 °C
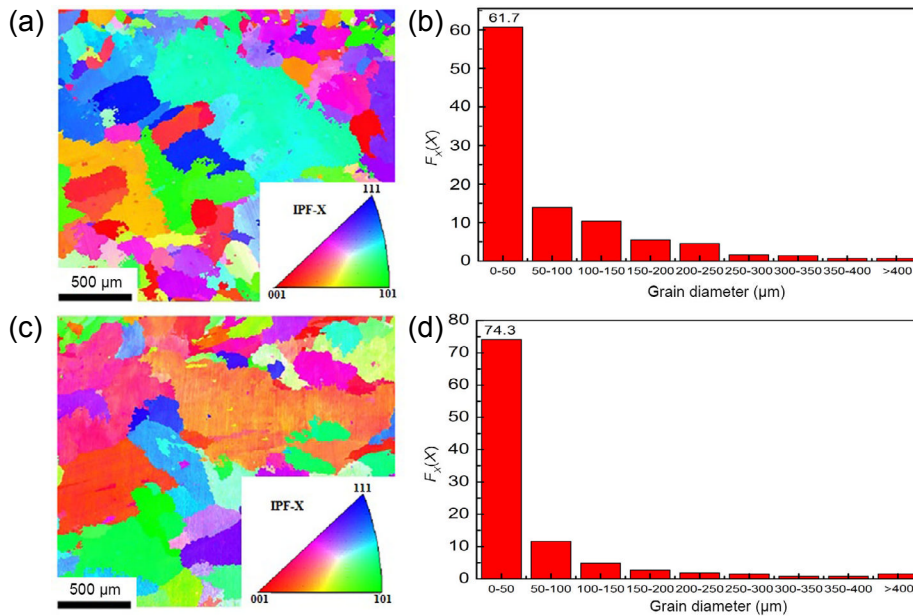

Fig. 11: EBSD maps (a, c) and distribution of grain size (b, d) of HEA coatings cladded (a, b) and annealed at 850 °C (c, d)

3.6 Discussion

During the plasma cladding process, the turbulent flow in the molten pool causes gas entrapment, and the rapid cooling also inhibits the escape of the gas from the molten pool [23], resulting in the formation of pores and micro-voids in all samples (Fig. 8). In addition, Mn has the lowest melting point among the main elements of CoCrFeMnNi HEA coating, and it is easily oxidized to form oxide particles during the cladding heating process [30]. The negative mixing enthalpy of C and the main elements of HEAs coating is shown in Table 7. It is observed that Mn and Cr have more negative enthalpy values, indicating that Mn or Cr carbides are most easily formed in the
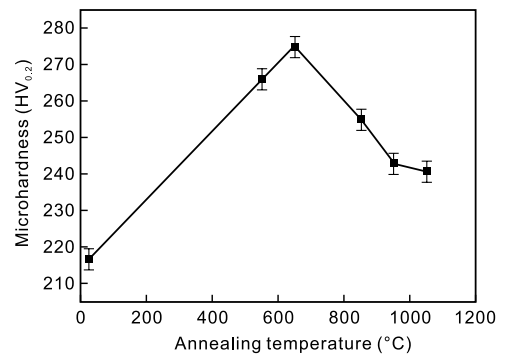

Fig. 12: Microhardness of surface of cladded and annealed CoCrFeMnNi HEA coatings
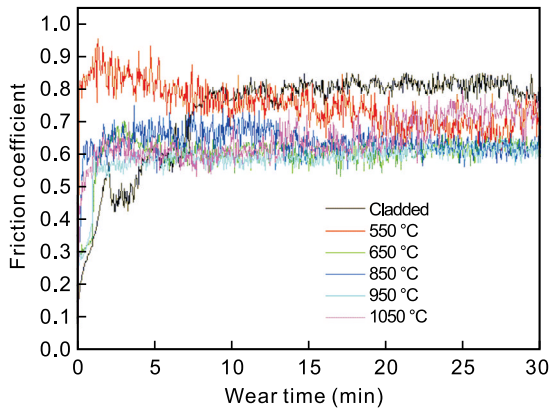
Fig. 13: Friction coefficient of cladded and annealed CoCrFeMnNi HEA coatings
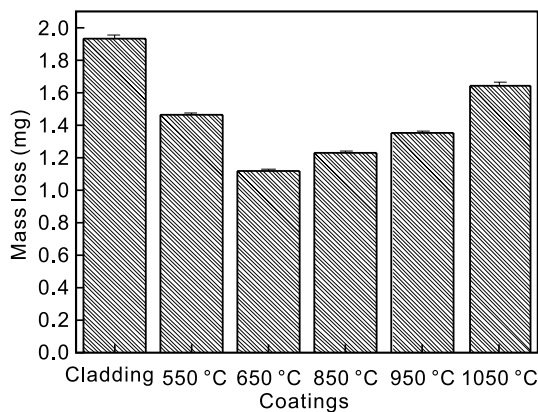

Fig. 14: Wear loss of cladded and annealed CoCrFeMnNi HEA coatings

CoCrFeMnNi HEA coating. Lin et al. [31] pointed out that it is easy to form $M_{23}C_6$ type (Cr, Mn) carbides during the preparation of $CoCrFeMnNiC_x$ HEAs. Moreover, Mn or Cr oxides show good wetting property with the carbide phases, providing a good heterogeneous nucleus for the carbide [32]. Thus, oxides and carbides easily concentrate on the CoCrFeMnNi HEA coating. That's why some aggregations consist many impurity elements such as C, O, Al, and Si (Areas A and C of Fig. 8). The atomic volume fraction of these impurity elements even reaches 59.6% in Area C in Fig. 8, as shown in Table 6. When the cladded coatings are properly annealed, the aggregations are more dispersed, and the content of impurity elements is higher [33].

The diffusion in HEAs is slower than that in conventional alloys due to the sluggish diffusion effect. Following annealing at 850 °C, the grain size in the CoCrFeMnNi HEA coating does not experience a rapid increase like other steel alloys. Most of the grains still remain around 50 μm in size, which is comparable to that of the cladded HEA coating (Fig. 11), indicating that the CoCrFeMnNi HEA coating has good stability of microstructure at high-temperature. This maybe attributed

Table 7: Values of mixing enthalpy of different atomic pairs with C

ΔH_{mix} (kJ·mol^{-1})	Co	Cr	Fe	Mn	Ni	Al
C		−42	−61	−42	−66	−39	−36

to the intrinsic characteristic of HEAs such as lattice distortion, sluggish diffusion, and polyatomic cooperative motion [23,34]. In particular, at the intermediate temperature annealing stage (600–900 °C), there is no main diffusion element in the coating, so that annealing twins, sub-grains and heterogeneous nucleation can inhibit the grain growth of the HEA coating [35].

The microhardness of CoCrFeMnNi HEA coatings increases at first and then decreases with an increase of annealing temperature. This can be explained as follows: Firstly, the crystalline structure of the coatings changes from FCC to BCC or FeCr phases during annealing. Simultaneously, due to precipitation strengthening and lattice distortion caused by the Cr-rich precipitation and BCC phases formation, the resistance of the dislocation motion increases [36], and thus the microhardness of the coatings is improved. However, the microhardness reduced gradually when the annealing temperature exceeds 650 °C. The decreased microhardness is attributed to the grain coarsening rather than the crystalline structure change from FCC to BCC or FeCr phases [23]. The relationship between grain size and the microhardness of FeCoNiCrMn HEA can be expressed by Hall-Petch equation [37]:

$$H=H_0+k_h d^{-1/2} \qquad (2)$$

where H is the microhardness, H_0 is the intrinsic microhardness, k_h is the Hall-Petch coefficient, and d is the average grain size. The microstructure evolution presented in Fig. 7 shows that when the annealing temperature exceeds 650 °C, the precipitation and grain size clearly rise with an increase in temperature. According to Eq. (2), the microhardness decreases with increasing grain size. This explains why the microhardness increases at first and then decreases as the annealing temperature increases. In addition, the hardness of the coating annealed at 1,050 °C is still higher than that of the cladded HEA coating, which is attributed to the dispersion strengthening caused by the dissolution or decomposition of carbides and oxides.

According to Archard's law [38], the wear resistance is positively related to the hardness of the materials. Moreover, as the annealing temperature increases, various wear mechanisms are observed in CoCrFeMnNi HEA coatings due to their microstructural evolution. According to previous observations [39], the dislocation of Cr segregation might be the reason for the precipitation of the Cr-rich phase. For the CoCrFeMnNi HEA coating cladded by micro-beam plasma, this strengthening effect is decreased due to the coarsening and the dissolution of the Cr-rich precipitations during the heat treatment process [19]. In this study, the wear resistance of the HEA coatings increases at first and then decreases with an increase in annealing temperature. Thus, the wear resistance of the HEA cladded coatings can be improved by annealing the coatings at a proper temperature range.

4 Conclusions

In this study, plasma cladding technology was employed to successfully prepare CoCrFeMnNi high entropy alloy coatings with stable structure and performances on Q235

steel. The process parameters were optimized by orthogonal method, and the microstructure and performance characteristics of high entropy alloy cladded coatings under the optimal process parameters were investigated systematically. The effects of annealing process on the microstructure and properties of the coatings were studied, and following conclusions are obtained:

(1) Based on the analysis of range, variance and surface morphology, the optimal process parameters combination is confirmed as the cladding current of 70 A, cladding speed of 7 cm·min^{-1}, and powder gas flow rate of 8 L·s^{-1}. The quality of the CoCrFeMnNi HEA coatings prepared by the optimized plasma cladding process is feasible.

(2) Some pores, micro-voids and aggregations could be observed in the cladded and annealed CoCrFeMnNi HEA coatings. The aggregations in the cladded coating are more concentrated, while they are more dispersed in the annealed coatings. The crystalline structure of the cladded coating mainly consists of the FCC phase, and a Cr-rich phase precipitates from the FCC matrix after annealed at a temperature range of 550–950 °C.

(3) After annealed at 850 °C, the proportion of the FCC phase in the cladded CoCrFeMnNi HEA coating is lower compared to before annealing. Additionally, there is a significant reduction in the number of large-angle grain boundaries. Moreover, there is an increase in the proportion of grains with sizes below 50 μm from 61.7% to 74.3%.

(4) The mechanical properties of the plasma cladded coatings could be significantly improved by annealing at a certain temperature range. The microhardness of the annealed CoCrFeMnNi HEA coating could be increased to 274.82 HV$_{0.2}$ after annealed at 650 °C, while the friction coefficient is decreased to below 0.595.

In general, this study has confirmed that CoCrFeMnNi HEA coatings with controllable microstructure and excellent mechanical properties can be prepared by a combination of plasma cladding and annealing treatment.

Acknowledgements

Conflict of interest

The authors declare that they have no known competing financial interests or personal relationships that could have appeared to influence the work reported in this paper.

References

[1] Li Z Z, Zhao S T, Ritchie R O, et al. Mechanical properties of high-entropy alloys with emphasis on face-centered cubic alloys. Progress in Materials Science, 2019, 102: 296–345.

[2] George E P, Curtin W A, Tasan C C. High entropy alloys: A focused review of mechanical properties and deformation mechanisms. Acta Materialia, 2020, 188: 435–474.

[3] Listyawan T A, Lee H, Park N, et al. Microstructure and mechanical properties of CoCrFeMnNi high entropy alloy with ultrasonic nanocrystal surface modification process. Journal of Materials Science & Technology, 2020, 57(22): 123–130.

[4] Jin G, Li Y, Cui X F, et al. Characterization of high-temperature mechanical properties of plasma-cladded coatings with thermo-mechanical coupling. Materials Characterization, 2018, 145: 196–204.

[5] Oukach S F, Pateyron B, Pawłowski L. Physical and chemical phenomena occurring between solid ceramics and liquid metals and alloys at laser and plasma composite coatings formation: A review. Surface Science Reports, 2019, 74(3): 213–241.

[6] Hariharan S J, Vigneshwar M, Selvamani S T, et al. Optimizing the plasma arc welding process parameters to attain the minimum corrosion rate in the AISI 409M grade ferritic stainless steel autogenous joints. Materials Today: Proceedings, 2019, 16: 1259–1270.

[7] Yuan Y L, Li Z G. Microstructure and tribology behaviors of in-situ WC/Fe carbide coating fabricated by plasma transferred arc metallurgic reaction. Applied Surface Science, 2017, 423(30): 13–24.

[8] Cheng J B, Liang X B, Wang Z H, et al. Formation and mechanical properties of CoNiCuFeCr high-entropy alloys coatings prepared by plasma transferred arc cladding process. Plasma Chemistry & Plasma Processing, 2013, 33(5): 979–992.

[9] Wei Y, Wei X S, Chen B, et al. Parameter optimization for tungsten carbide/Ni-based composite coating deposited by plasma transferred arc hardfacing. Transactions of Nonferrous Metals Society of China, 2018, 28 (12): 2511–2519.

[10] Wang D Y, Lai Y B, Li X, et al. Influence of process parameter on the residual stress of multi-track overlapping plasma cladding. Vacuum, 2019, 56(6): 80–84.

[11] Li X, Lai Y B, Yang B, et al. Process optimization and properties of Fe-Cr-C alloy coating prepared by plasma cladding. Surface Technology, 2020, 49(6): 177–184.

[12] Lu J B, Wang B F, Qiu X K, et al. Microstructure evolution and properties of CrCuFexNiTi high entropy alloy coating by plasma cladding on Q235. Surface & Coatings Technology, 2017, 328: 313–318.

[13] Lu B W, Cui X F, Li Y, et al. Microstructure, bonding properties and the basis of pinning effect of in-situ NbC reinforced Co50 composite coating by plasma cladding. Surface & Coatings Technology, 2017, 319: 155–163.

[14] Otto F, Dlouhy A, Pradeep K G, et al. Decomposition of the single-phase high entropy alloy CrMnFeCoNi after prolonged anneals at intermediate temperatures. Acta Materialia, 2016, 112: 40–52.

[15] Sathiyamoorthi P, Asghari-Rad P, Karthik G M, et al. Unusual strain-induced martensite and absence of conventional grain refinement in twinning induced plasticity high-entropy alloy processed by high-pressure torsion. Materials Science and Engineering: A, 2021, 803: 140570.

[16] Wang P, Chen J, Sun B, et al. Effects of annealing process parameters on microstructural evolution and strength-ductility combination of CoCrFeMnNi high-entropy alloy. Materials Science & Engineering: A, 2022, 840: 142880.

[17] Liu J L, Yu H J, Chen C J, et al. Research and development status of laser cladding on magnesium alloys: A review. Optics and Lasers in Engineering, 2017, 93: 195–210.

[18] Hao H, Liu J, Li X, et al. Effect of heat treatment on phase stability and wear behavior of laser clad AlCoCrFeNiTi$_{0.8}$ high-entropy alloy coatings. Surface & Coatings Technology, 2020, 392: 125758.

[19] Feng G C. Influencing factors and control measures of dilution rate of surfacing welding. Welding Technology, 1996, 25(1): 22–24.

[20] Ye F X, Jiao Z P, Yuan Y H. Precipitation behaviors and properties of micro-beam plasma arc cladded CoCrFeMnNi high-entropy alloy at elevated temperatures. Materials Chemistry and Physics, 2019, 236: 121801.

[21] He F, Wang Z, Wu Q, et al. Phase separation of metastable CoCrFeNi high entropy alloy at intermediate temperatures. Scripta Materialia, 2017, 126: 15–19.

[22] Ming K S, Bi X F, Wang J. Microstructures and deformation mechanisms of Cr26Mn20Fe20Co20Ni14 alloys. Materials Characterization, 2017, 134: 194–201.

[23] Tong Z P, Ren X D, Jiao J F, et al. Laser additive manufacturing of FeCrCoMnNi high-entropy alloy: Effect of heat treatment on microstructure, residual stress and mechanical property. Journal of Alloys and Compounds, 2019, 785: 1144–1159.

[24] Zhang Q, Wang Q, Han B, et al. Comparative studies on microstructure and properties of CoCrFeMnNi high entropy alloy coatings fabricated by high-speed laser cladding and normal laser cladding. Journal of Alloys and Compounds, 2023, 947: 169517.

[25] Sun M, Wang B W, Zhang J X, et al. In-situ synthesis of CoCrFeMnNi high-entropy alloy by selective laser melting. Intermetallics, 2023, 156: 107866.

[26] Weng Z Q, Dong G, Zhang Q L, et al. Effects of annealing on microtrucre and properties of FeCrNiCoMn high entropy alloy coating prepared by laser cladding. Chinese Journal of Lasers, 2014, 41(3): 59–64.

[27] Wei C L, Chang Y J, Hu T H, et al. Microstructure and tensile property of a precipitation strengthened high entropy alloy processed by selective laser melting and post heat treatment. Additive Manufacturing, 2020, 36: 101601.

[28] Shahmir H, He J Y, Lu Z P, et al. Effect of annealing on mechanical properties of a nanocrystalline CoCrFeNiMn high-entropy alloy processed by high-pressure torsion. Materials Science & Engineering: A, 2016, 676: 294–303.

[29] Li X F, Feng Y H, Liu B, et al. Influence of NbC particles on microstructure and mechanical properties of AlCoCrFeNi high-entropy alloy coatings prepared by laser cladding. Journal of Alloys and Compounds, 2019, 788: 485–494.

[30] Yao M J, Pradeep K G, Tasan C C, et al. A novel, single phase, non-equiatomic FeMnNiCoCr high-entropy alloy with exceptional phase stability and tensile ductility. Scripta Materialia, 2014, 72–73: 5–8.

[31] Lin G, Ou X Q, Song N, et al. Effects of carbon on the microstructures and mechanical properties of FeCoCrNiMn high entropy alloys. Materials Science & Engineering: A, 2019, 746: 356–362.

[32] Wang H L, Guo Y X, Lan H W, et al. Effect of spot type on microstructure and properties of MoFeCrTiWAlNb refractory high-entropy alloy coating fabricated by laser cladding. Surface Technology, 2019, 48(6): 130–137.

[33] Munitz A, Salhov S, Hayun S, et al. Heat treatment impacts the micro-structure and mechanical properties of AlCoCrFeNi high entropy alloy. Journal of Alloys and Compounds, 2016, 683: 221–230.

[34] Wang A J, Wu A S, Fu S, et al. Itrahigh hardness with exceptional thermal stability of a nanocrystalline CoCrFeNiMn high-entropy alloy prepared by inert gas condensation. Scripta Materialia, 2020, 187: 335-339.

[35] Xiao L L, Zheng Z Q, Guo S W, et al. Ultra-strong nanostructured CrMnFeCoNi high entropy alloys. Materials & Design, 2020, 194: 108895.

[36] Fu J X, Cao C M, Tong W, et al. The tensile properties and serrated flow behavior of a thermomechanically treated CoCrFeNiMn high-entropy alloy. Materials Science & Engineering: A, 2017, 690: 418–426.

[37] Liu W H, Wu Y, He J Y, et al. Grain growth and the Hall-Petch relationship in a high-entropy FeCrNiCoMn alloy. Scripta Materialia, 2013, 68: 526–529.

[38] Guo Y X, Shang X J, Liu Q B. Microstructure and properties of in-situ TiN reinforced laser cladding CoCr$_2$FeNiTi$_x$ high-entropy alloy composite coatings. Surface & Coatings Technology, 2018, 344: 353–358.

[39] Zhou W, Fu L M, Liu P, et al. Deformation stimulated precipitation of a single-phase CoCrFeMnNi high entropy alloy. Intermetallics, 2017, 85: 90–95.